Design of quantum dot networks for improving prediction performance in reservoir computing

KAZUKI YAMANOUCHI,[1,*] SUGURU SHIMOMURA,[1] AND JUN TANIDA[1]

[1]*Graduate School of Information Science and Technology, Osaka University, 1–5 Yamadaoka, Suita, Osaka 565–0871, Japan*
[*]*k-yamanouchi@ist.osaka-u.ac.jp*

Abstract:

A quantum dot (QD) network generates various fluorescence signals based on nonlinear energy dynamics, which depend on its structure and composition, and is utilized as a component in physical reservoir computing. However, existing designs rely on random QD networks, which are not optimal for enhancing the prediction performance. In this paper, we propose a method for designing effective quantum dot networks to improve the performance of reservoir computing. The fluorescence signals from numerous virtual QD networks can be reproduced through numerical simulation based on a deterministic mathematical model, and the QD networks generating the most significant signals contributing to the prediction performance are identified. We demonstrated that QD reservoir computing using designed QD networks predicts time-series data more accurately than using random QD networks in the numerical simulations.

1. Introduction

Quantum dots (QDs), which are nanoscale phosphors, are utilized across various fields including sensing and imaging [1, 2]. The diameter-dependent band gap of QDs allows for easy tuning of the peak fluorescence wavelength [3]. By synthesizing QDs that emit light in the near-infrared region to mitigate biological scattering effects, 3D imaging of tumor blood vessels up to a depth of 1.2 mm is achieved [4]. Moreover, the absorption spectra of QDs are broader than those of other organic phosphors, enabling dual-emission and single-excitation labeling experiments in mouse fibroblasts [5, 6].

Förster resonance energy transfer (FRET), which occurs between phosphors such as QDs, is a crucial functionality of QDs [7, 8]. FRET efficiency is contingent upon the donor-acceptor combination and their proximity. When phosphors are closely packed, the excited energy is sequentially transferred through FRET [9], facilitating energy dynamics crucial for multi-step FRET applications in nanoscale information processing. For instance, fluorescent molecules arranged on DNA through multi-step FRET have facilitated nanoscale logic operations [10]. Complex arithmetic circuits, such as half adders and subtractors, were implemented using temporally varying FRET pathways between different phosphors [11]. Viewing multi-step FRET as a natural continuous-time Markov chain allows the construction of units that generate samples conforming to various probability distributions in probabilistic computing [12]. The strategic arrangement of QDs to generate FRET-modulated fluorescence signals enables nanoscale computing.

A QD network comprises multi-step FRET in a structure where randomly distributed QDs generate fluorescence signals contingent on their configuration. When pulsed lights are sequentially irradiated, the excited energy in QDs is retained through multistep FRET, accumulating past input pulses within the network. The resultant fluorescence signals exhibit nonlinear responses based on the intensity and timing of the pulse sequences [13, 14].

Additionally, the fluorescence signals can be modulated by changing the spatial distribution of the QDs. For instance, during electrophoretic deposition, the deposition time has been found to influence the distribution of deposited QDs [15]; further, physically flexing the substrate with QDs change the distances between QDs [16], thereby modulating the fluorescence signals.

By using lithographic techniques to fabricate a structure containing excitation paths formed by randomly distributed QDs, useful fluorescence responses for nanophotonic devices have been achieved [17].

The nonlinear signals of QD networks, modulated by temporal pulse sequences, are essential for physical reservoir computing, which processes time-series data. Previously, we constructed QD reservoir computing (QDRC) using QD networks as a reservoir layer and demonstrated its capability to predict time-series signals of 1 bit delay XOR tasks with low mean squared errors [15].

Photonic reservoir computing has been explored previously using various approaches, including passive silicon photonics [18] and time-delayed lasers [19]. Compared to these methods, the advantage of QDRC lies in the size of the system. A physical reservoir that uses QD networks is based on light irradiation and energy transfer. Because of the connections without wiring and the nanoscale size of the QD, it is possible to significantly reduce the size of the physical reservoir. Furthermore, parallel processing of multiple time-series data can be achieved through spatial multiplexing of the pulse sequences.

The prediction performance depends on the distribution and composition ratio of multiple QDs. To utilize QD networks as reservoirs, they need to generate characteristic signals suitable for prediction. QD networks can generate a variety of fluorescence signals depending on the energy dynamic of the QDs through FRET. However, randomly dispersing QDs result in a variety of structures that are not unique, which causes signals with similar characteristics to be generated. Previous studies have shown that external mechanical manipulation can change the overall spatial distribution of QDs and modulate the fluorescence signal. Nevertheless, the potential differences in energy dynamics between locally existing QD networks have not been fully explored. Reservoir computing performance can be enhanced by optimizing the topology of the reservoir layer [20]. By identifying QD networks that generate characteristic signals, we can unlock the potential of QD networks in reservoir computing, which has been obscured by randomness, and broaden the range of prediction tasks that QDRC can handle.

We propose a method for designing QD networks that generate signals to enhance the prediction performance of QDRC. To achieve this, a deterministic mathematical model of the QD network using the rate equation is constructed. Although several methods can reproduce the energy dynamics of fluorophores in simulations [21,22], they are not suitable for simulating signals from numerous QD networks due to the extensive computational time required by iterative sampling based on Monte Carlo simulation. A deterministic algorithm allows for the reproduction of energy dynamics in the QD network without randomness, generating fluorescence signals from a large number of QD networks. Utilizing this model, we designed QD networks that produce significant signals contributing to prediction performance. Finally, we evaluated the prediction performance of time-series signals using the QDRC designed by the proposed method.

2. Quautum dot reservoir computing

In QDRC, the reservoir layer is constructed using an ensemble of QD networks. Multistep FRETs induce the energy dynamics of QDs, and the QD networks generate nonlinear fluorescence signals depending on the irradiation conditions. Figure 1 shows a schematic of the proposed QDRC. In the input layer, time-series data is converted into a sequence of optical pulses, with data values encoded in the peak intensity of these pulses. These encoded pulses are duplicated and irradiated onto randomly distributed QDs. The light energy is absorbed by the QDs and retained within the QD ensemble through multistep FRETs. Each QD is interconnected via energy transfers, forming the QD networks that constitute the reservoir layer. Within this network, the level occupancy effect, induced by energy absorption and saturation, generates nonlinear responses with short-term memory due to energy dynamics, facilitating information

processing [15]. In the output layer, signals generated by each QD network are captured, and the output is obtained by weighting individual signals. These weights are optimized by linear regression methods such as ridge regression. The prediction performance relies on the output signals from individual QD networks; thus, the design of QD networks enhances the capability of information processing.

However, the design process requires validations of QD networks and iterative acquisition of fluorescence signals. In this study, we implemented numerical simulation using a mathematical model of the QDs and evaluated fluorescence signals generated from a large number of virtually constructed QD networks.

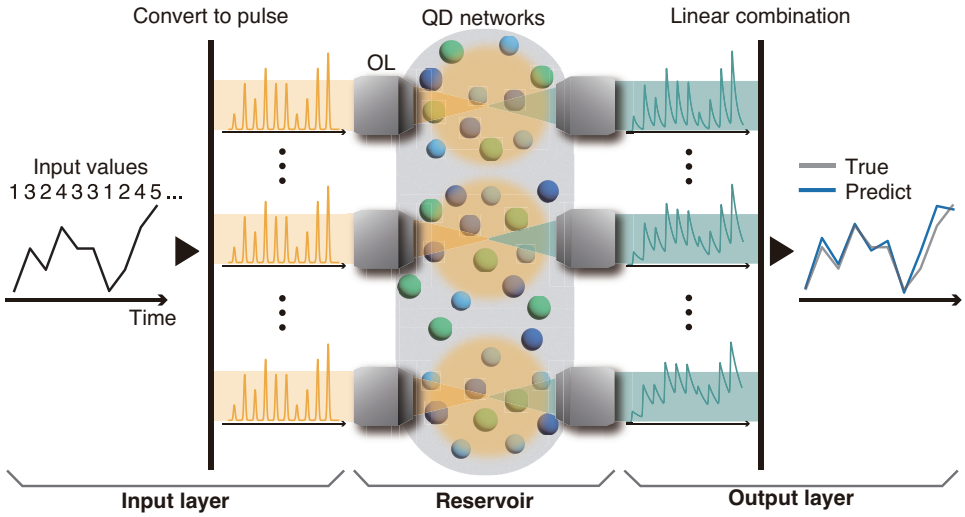

Fig. 1. Schematics of quantum dot reservoir computing. OL:Objective lens.

3. Mathematical model of quantum dot networks

3.1. Rate equation of QDs

To reproduce the fluorescence signals generated by a large number of QD networks, we construct a mathematical model of electron transitions within individual QDs using a deterministic approach. Previous models have assumed that electrons in a QD transition between multiple energy levels [23–25]. We develop a two-level system for electrons in QDs, incorporating FRET and level occupancy effects. Figure 2 shows a Jablonski diagram representative of the QD networks. The number of electrons in the ground and excitation levels are denoted as S_g and S_e, respectively. The total number of electrons within the QD remains constant $S(= S_e + S_g)$. The rate equations for the excited electrons in the i-th QD, considering FRET and level occupancy effects, are expressed as follows:

$$\frac{dS_{e,i}}{dt} = \frac{\sigma_i^{\mathrm{abs}} I_{ex}(t)}{h\nu_i} S_{g,i} - k_{nr,i} S_{e,i} - k_{r,i} S_{e,i} - \sum_{i \neq j} k_{i \to j} S_{e,i} + \frac{S_{g,i}}{S_i} \sum_{i \neq j} k_{j \to i} S_{e,j}. \quad (1)$$

Here, $I_{ex}(t), h, \sigma_i^{\mathrm{abs}}$, and ν_i represent the irradiated photon density at time t, Planck's constant, the absorption cross-section, and the fluorescence frequency of the i-th QD, respectively. $k_{r,i}$ and $k_{nr,i}$ are the rate constants for the radiative and non-radiative relaxation processes, given by $k_{r,i} = Q_i/\tau_i, k_{nr,i} = (1 - Q_i)/\tau_i$. Q_i is the quantum yield and τ_i is the fluorescence lifetime. The first term in the rate equation (Eq. (1)) accounts for optical excitation, with the number

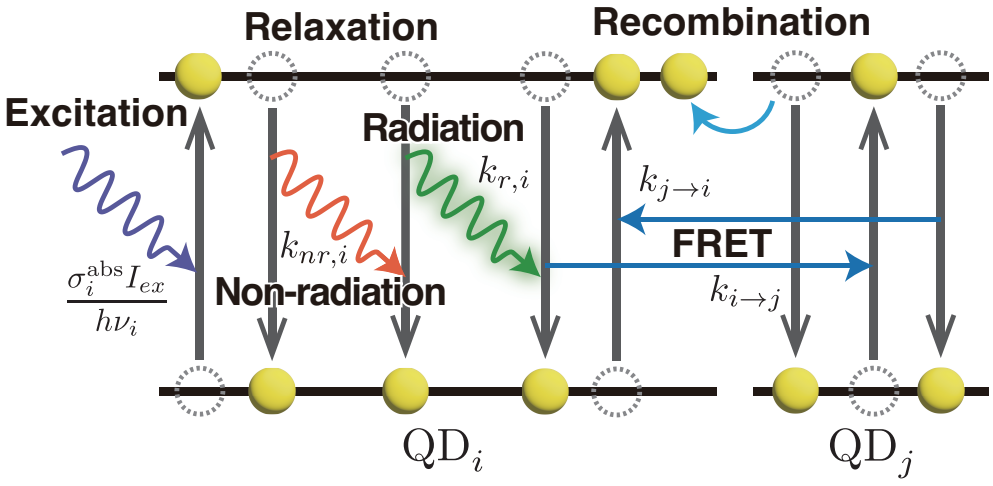

Fig. 2. A Jablonski diagram of the QDs in the QD network.

of electrons transitioning to the excitation level dependent on those in the ground level, $S_{g,i}$. The second and third terms describe the energy emission through radiative and non-radiative relaxation processes, respectively, with the transition probability dependent on the number of excited electrons, $S_{e,i}$. The fourth and fifth terms detail the FRET interactions between the i-th and j-th QDs. FRET is explained by Förster's theory [7], and its mathematical model is detailed in Ref. [26]. Based on these theories and mathematical models, the rate constant of FRET is expressed as

$$k_{i\to j} = \frac{1}{\tau_i}\left(\frac{R_0(i,j,\kappa,n)}{R(i,j)}\right)^6, \tag{2}$$

where $R(i,j)$ is the distance between the i-th and j-th QDs. $R_0(i,j,\kappa,n)$ the Förster distance, is a constant that depends on the QD type (i,j), orientation factor κ, and refractive index n [7]. The fifth term in Eq. (1) indicates the level occupancy effect, such as Auger recombination, induced by FRET. When more electrons are in the excited state, Auger recombination is triggered, causing electrons in the acceptor QD to transition to a higher energy level and subsequently return to their original energy state through a non-radiative relaxation process [23, 27]. This return to the original level typically occurs within a few picoseconds [28]. In two-level systems, electronic transitions through Auger recombination are rapid, and the excited electrons in the acceptor remain in the excited state. The excitation energy received from other QDs by FRET is lost through non-radiative recombination, which depends on the number of electrons in the excited state. Consequently, the transition probability due to FRET varies based on the number of electrons in the ground state, leading to nonlinear energy dynamics within the QDs.

The fluorescence signal from the QD network is the sum of the radiation energies from each QD. The signal intensity $f(t)$ can be expressed as

$$f(t) = \sum_i (k_{r,i} S_{e,i}(t) \times h\nu_i). \tag{3}$$

Eq. (3) implies that the time-series fluorescence signal depends the number of electrons of the QD at time t. The fluorescence signal generated by the QD network can be reproduced when a sequence of pulses is irradiated using Eq. (1) – (3). Moreover, a deterministic algorithm based

on the Euler method enables the calculation of the fluorescence signal without numerous trials. Thus, the fluorescence signals from various QD networks can be reproduced, facilitating the numerical simulation of QDRC.

3.2. Evaluation of rate equation

Fluorescence decay under various irradiation conditions and types of QD samples was observed when pulsed light was irradiated on a QD ensemble [13]. The observed signal featured a multi-component exponential decay of fluorescence. The decay rate of fluorescence increases with higher QD density or irradiation intensity. To verify the proposed model of the QD network, we compared the fluorescence decay generated by numerical simulations with experimental results. Table 1 lists the physical parameters used for the simulations. QD networks were prepared by mixing QDs into polydimethylsiloxane (PDMS) and spreading them on a slide glass [14]. The refractive index n was set to that of PDMS. The orientation factor κ^2 was set to $2/3$, which is the dynamic isotropic average of κ^2, assuming that the QDs were randomly dispersed and the orientations of QDs were within the dynamic averaging regime. The excitation wavelength was set at 400 nm, and the pulse width was adjusted according to the measured light intensity of the pulsed laser used in the experiment. Table 2 shows the values of the QD parameters. Förster distances between the three types of QDs are illustrated in Fig. 3. These QD parameters were derived from the experimental measurements of QD samples (QD490: 753904, Sigma-Aldrich; QD540 and QD 580: CZ540 and CZ580, NN-labs, LLC).

Table 1. Physical parameters in the simulation.

Parameter	Value
n	1.44
κ^2	$2/3$
Excitation wavelength	400[nm]
Pulse width in time domain	74[ps]

We assumed that the QD network can be regarded as QDs distributed in three-dimensional space. The network comprises 20 QDs, with their positions following a three-dimensional normal distribution with a standard deviation s, corresponding to the density of the QDs. We generated one thousand types of QD networks consisting solely of QD580, while varying the standard deviation between 8 and 200 nm.

Figure 4 shows the simulated fluorescence signals under irradiation of the generated QD networks with a single pulse of light. Individual signal is normalized by the value at time $t = 0$. The simulated fluorescence intensity decreased exponentially, which reproduced the behavior of the fluorescence decay. Under an irradiation intensity of 1.0×10^5, the difference of the decay depending on the standard deviation s of QDs' spatial distribution is shown in Figure 4(a). Furthermore, the decay was swifter in case of the intensity of 2.0×10^6 [Figure 4(b)]. To evaluate the decay, we measured the average and standard deviation of time $t_{1/e}$ at which the normalized intensity reached $1/e$. While $t_{1/e}$ was 7.27±0.41 ns in case of weak intensity, it was 6.42 ± 0.87 ns in case of high intensity. Moreover, the decay in case of the intensity of 2.0×10^6 was speedier under smaller values of s. The simulation result shows non-single exponential decay, which corresponds with a previous result [13, 21]. We have confirmed that our model reproduces the fluorescence signals of the QD network.

Table 2. QD parameters in the simulation. Absorption cross section values σ^{abs} are shown for the irradiation wavelength of 400 nm.

Parameter	QD type		
	QD490	QD540	QD580
Q	0.40	0.40	0.40
τ [ns]	9.4	8.6	7.9
ν [Hz]	6.1×10^{14}	5.6×10^{14}	5.2×10^{14}
σ^{abs} [cm^2]	2.1×10^{-16}	1.3×10^{-17}	1.6×10^{-17}
$k_r = Q/\tau$ [1/s]	4.3×10^{7}	4.7×10^{7}	5.1×10^{7}
$k_{nr} = (1-Q)/\tau$ [1/s]	6.4×10^{7}	7.0×10^{7}	7.6×10^{7}
$N = 1/\tau$	1.1×10^{8}	1.2×10^{8}	1.3×10^{8}

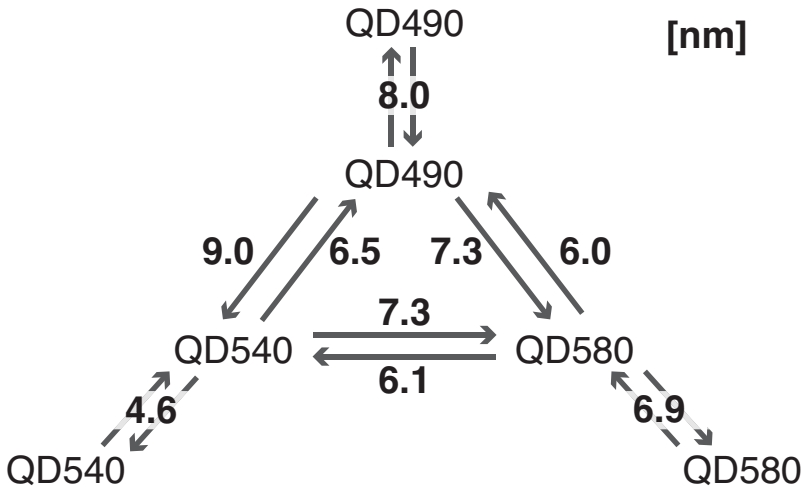

Fig. 3. Förster distances between the three types of QDs. The units of each value are in nanometers.

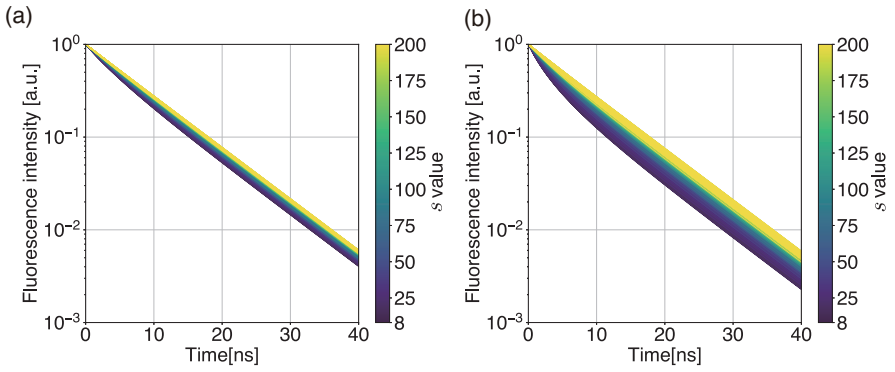

Fig. 4. Fluorescence signals generated by 1,000 types of QD networks. The position of the QDs follows three-dimensional normal distribution, and s represents the standard deviation of its distribution. (a) Irradiation intensity: $1.0 \times 10^5 [\mathrm{W/cm^2}]$ (Weak excitation). (b) Irradiation intensity: $2.0 \times 10^6 [\mathrm{W/cm^2}]$ (Strong excitation).

4. Design of effective quantum dot networks

4.1. Rank evaluation of fluorescence signal and selection of QD network

To enhance prediction performance, it is necessary to generate the signals that contribute significantly to the prediction. In RC, the orthogonality of outputs from the reservoir layer is crucial for prediction performance and is employed as a performance metric [29–31]. To design QD networks that enhance the performance of QDRC, we evaluated the rank of a matrix composed of fluorescence signals. The temporal output from the QDRC is denoted as $y_{\mathrm{out}}(t)$ $(t = 1, \ldots, T)$. The output is expressed by

$$\hat{\boldsymbol{y}}_{\mathrm{out}} = \boldsymbol{F}\boldsymbol{w}, \tag{4}$$

where $\hat{\boldsymbol{y}}_{\mathrm{out}} = (y_{\mathrm{out}}(1), \ldots, y_{\mathrm{out}}(T))^\top$ and the matrix $\boldsymbol{F} = (\boldsymbol{f}_1, \ldots, \boldsymbol{f}_N)$ consists of the time-series signals generated by the n-th QD network, written by $\boldsymbol{f}_n = (f_n(1), \ldots, f_n(T))^\top$ $(n = 1, \ldots, N)$. $\boldsymbol{w} = (w_1, \ldots, w_N)^\top \in \mathbb{R}^N$ is an N-dimensional weight vector, and the dimension of a vector space $\mathcal{Y}$ containing the output $\hat{\boldsymbol{y}}_{\mathrm{out}}$ is determined by the rank of the matrix $\boldsymbol{F}$ $\left(\dim \mathcal{Y} = \dim(\mathrm{Im}\, F) = \mathrm{rank}\, \boldsymbol{F},\ \mathrm{Im}\, F = \{\hat{\boldsymbol{y}}_{\mathrm{out}} \in \mathbb{R}^T \mid \exists \boldsymbol{w} \in \mathbb{R}^N, \hat{\boldsymbol{y}}_{\mathrm{out}} = \boldsymbol{F}\boldsymbol{w}\}\right)$. When the dimension of $\mathcal{Y}$ is higher, the prediction accuracy of reservoir computing improves. We define signals with a high rank of matrix $\boldsymbol{F}$ as 'effective' signals, leading to enhanced prediction performance of the QDRC. Networks generating such signals are termed effective QD networks. Initially, we generated N virtual QD networks, each containing L types of QDs with a total count of M QDs. We posited that these networks cluster within the QD sample, and the spatial distribution $\boldsymbol{r}_{n,m}$ of the m-th QD in the n-th network was set to follow the three-dimensional normal distribution: $\boldsymbol{r}_{n,m} \sim \mathcal{N}_3(\boldsymbol{0}, s_n \boldsymbol{E})$, where s_n denotes the standard deviation of the normal distribution, and $\boldsymbol{E}$ is the identity matrix. Subsequently, we simulated fluorescence signals from these networks upon irradiation with pulsed light. Among the signals generated by the virtual QD networks $\boldsymbol{f}_1, \ldots, \boldsymbol{f}_N$, we obtained a pair $\{\boldsymbol{f}_p, \boldsymbol{f}_q\}$ with the maximum Euclidean distance $d_{\max} = \|\boldsymbol{f}_p - \boldsymbol{f}_q\|_2^2$. In linear regression, optimization through extensive weighting is costly. To design QD networks that enable prediction, we choose K number of signals, such that the value of Euclidean distance from $\boldsymbol{f}_p$ or $\boldsymbol{f}_q$ is closest to $\{0, d_{\max}/2K', 2d_{\max}/2K', \ldots, (K'-1)d_{\max}/2K'\}$ where $K' = \left\lfloor \frac{K}{2} \right\rfloor$. The selected signals exhibited diverse fluorescence decay, characterizing nonlinear responses with varying short-term memory due to energy dynamics. From these, we derived the structures for the designed virtual QD network. The number of QDs in each network was set at $M = 20$, with three types of QDs (QD490, QD540, and QD580) in equal

proportions ($L = 3$). The properties of QD490, QD540, and QD580 used in the numerical simulations are listed in Table 2, and the Förster distances between the QDs are shown in Fig. 3. The QDs were distributed in three-dimensional space with standard deviations ranging from 8 to 200 $\left(s_n = 8 + \dfrac{200-8}{3000}(n-1)\right)$. A total of 3000 QD network types, each with a unique s_n, were simulated, and fluorescence signals at an irradiation intensity of $I = 1.0 \times 10^5$ were generated. With K set to 28, the rank of the signal matrix was evaluated. Figure 5 (a) displays the 3,000 types of signals generated in the simulation and the 28 signals selected. To evaluate the proposed algorithm, we used the Python library Numpy to analyze the ranks of matrices. Figure 5 (b) presents a histogram of the ranks for the matrix $\boldsymbol{F}_{\text{random}}$ consisting of 28 randomly selected signals. The numerical error tolerance was set at the maximum singular value of the matrix $\boldsymbol{F}$ multiplied by its higher dimension size of $\boldsymbol{F}$ and the machine epsilon. The average rank in 1,000,000 trials was 21.6, with the ranks of $\boldsymbol{F}_{\text{random}}$ ranging from 20 to 23 with a probability of 98.8 %. Outliers were identified using the two-sigma rule, assuming a rank distribution obtained over 1,000,000 trials. A red dashed line marks the rank of the matrix $\boldsymbol{F}_{\text{design}}$, composed of the selected signals, which was 26, matching that of the matrix $\boldsymbol{F}_{\text{all}}$, comprising all generated signals. These results demonstrate that the proposed method effectively selects signals for the matrix $\boldsymbol{F}_{\text{design}}$ with a high rank.

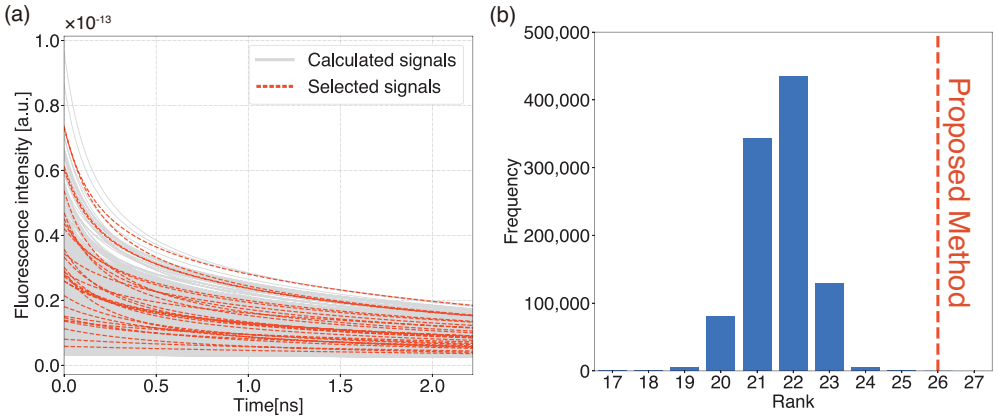

Fig. 5. (a) Calculated signals generated from 3,000 types of QD networks and 28 types of QD networks. (b) Frequency distribution of the ranks of matrix $\boldsymbol{F}_{\text{random}}$. The red dash line indicates the rank of matrix $\boldsymbol{F}_{\text{design}}$.

4.2. Performance evaluation

Next, we verified that the designed QD networks enhanced prediction accuracy. For benchmark tasks of signal prediction, we employed the Mackey-Glass equation, Santa Fe time-series data, and Nonlinear AutoRegressive Moving Average (NARMA) data [32–34]. The Mackey-Glass equation is expressed as follows,

$$\frac{dx(t)}{dt} = -ax(t) + \frac{bx(t-\tau)}{c + x(t-\tau)^n}, \tag{5}$$

where a, b, c, and n are constants, and τ is the delay time. The Mackey-Glass equation exhibits chaotic behavior depending on specific parameters. In our simulations, we set individual parameters to $a = 0.1$, $b = 0.2$, $c = 1$, $n = 10$, and $\tau = 17$ to generate a chaotic signal. The Santa Fe time series data, which consist of intensity data recorded from a far-infrared laser in a

chaotic state, are used in this study normalized by the maximum value. The m-order NARMA model is written as

$$x(t+1) = a_1 x(t) + a_2 x(t) \sum_{i=0}^{m-1} x(t-i) + a_3 u(t-m)u(t) + a_4. \tag{6}$$

Here, a_1, a_2, a_3, and a_4 are constants, and $u(t)$ represents the temporal input. The parameters were set to $m = 2$ and $a_1 = 0.3$, $a_2 = 0.05$, $a_3 = 1.5$, and $a_4 = 0.1$. The $u(t)$ values were independently and identically drawn from a uniform distribution within the interval $[0, 0.5]$. These time-series data were encoded into pulse sequences and input into each designed QD network. The frequency of the input signal was set to 1.0 GHz. Based on Eq. (4), the output was obtained by the linear summation of the generated signals. The weights $\boldsymbol{w}$ were optimized using ridge regression. For the prediction of the Mackey-Glass equation and Santa Fe time-series data, a one-step-ahead prediction approach was employed, where the input one step ahead is predicted from the reservoir state at each time step. In the case of the NARMA data, the output $x(t+1)$ represented the target signals and was predicted from the fluorescence signals when the input was $u(t)$. A dataset comprising 1200 steps of time-series data was utilized for optimization, and 600 steps of untrained data was used. To evaluate the performance, the normalized mean square error (NMSE) was employed as follows:

$$\mathrm{NMSE} = \frac{\sum_t \left(y(t) - y_{\mathrm{out}}(t)\right)^2}{\sum_t \left(y(t) - \bar{y}\right)^2}, \tag{7}$$

where $y(t), \bar{y}$ represents the target signal value and its average value, and $y_{\mathrm{out}}(t)$ is the output value by QDRC. Figures 6 (a-c) illustrate the relationship between the rank of the matrix $\boldsymbol{F}$, constructed using the QD networks and the NMSE. The simulation trial using non-designed QD networks was conducted 50 times, with each trial featuring different network structures. The rank of the matrix $\boldsymbol{F}_{\mathrm{design}}$ in the case of the designed QD networks was 26, $\boldsymbol{F}_{\mathrm{random}}$whereas for the non-designed QD networks, the rank of the matrix ranged from 20 to 23. The average NMSE decreased with increasing rank when using non-designed QDRCs; nonetheless, the NMSE of the QDRC employing designed QD networks was the lowest. These results indicate that the design of the QD network enhances the prediction performance of the QDRC. However, certain prediction results using non-designed QD networks were better than those using designed ones, particularly in the Santa Fe time-series data and NARMA data. We investigated the performance of the QDRC using individual combinations of the QD networks. Figure 6 (d) displays the relationship of the NMSE between the Santa Fe and NARMA tasks using the QDRC with a matrix $\boldsymbol{F}_{\mathrm{random}}$ rank of 23. The orange and green lines represent the NMSE in QDRC using the designed QD network (designed QDRC). While the QDRC using the non-designed QD network predicted one time-series data with a higher NMSE, its performance in the prediction of the other data was inferior compared with that using designed QD networks. The correlation coefficient between the NMSE values for the two tasks was 0.031, indicating no significant correlation between the prediction performances for the two tasks. This result suggests that the prediction performances of the QDRC using non-designed QD networks vary depending on the tasks. The NMSE of the designed QDRC in both tasks was better, demonstrating that the design of the QD networks contributes to the prediction performance across a broad range of tasks.

We discuss short-term memory, an important property of reservoir computing. In QDRC, the information of input signals is retained in the network through FRET and is eventually lost via relaxation processes. Therefore, memory capacity, which is a measure of the short-term memory, is related to the fluorescence decay of the QD network. Based on the definition in Ref. [35], we estimated the memory capacity of the designed QDRC. We used a 500-step random sequence as input, with each input value being a random number following a uniform distribution

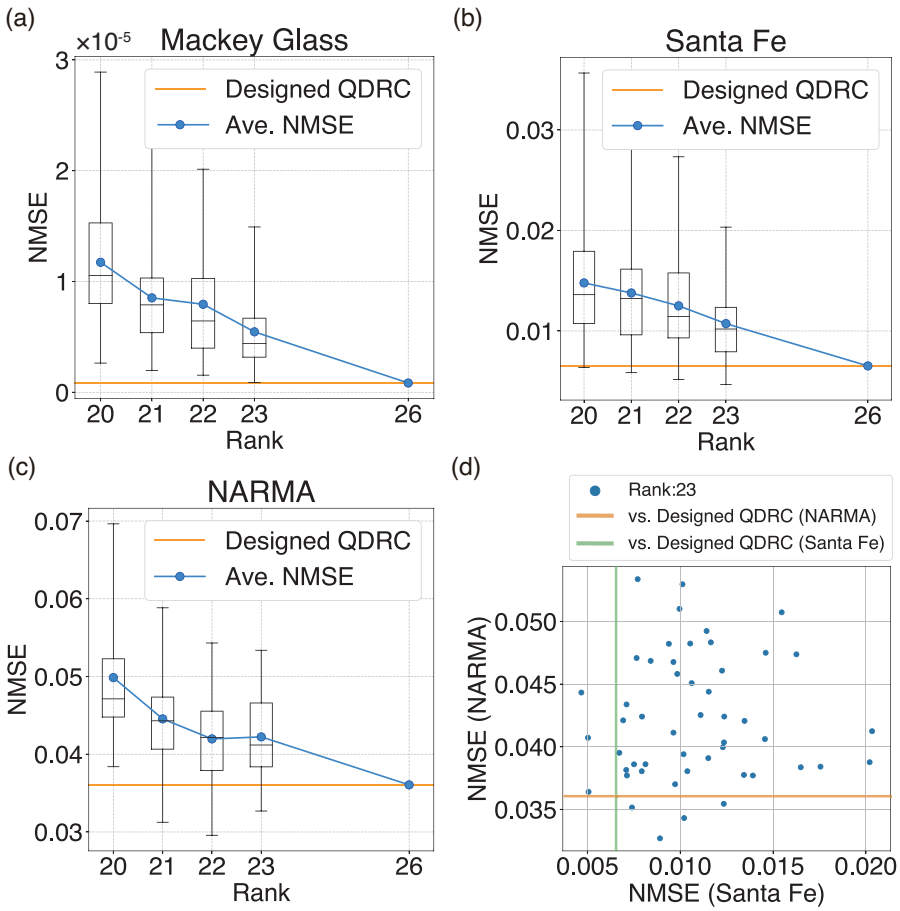

Fig. 6. Dependence of NMSE of the designed QDRC and the others on the rank of the matrix $\boldsymbol{F}$. (a) Mackey-Glass equation task. (b) Santa Fe task. (c) NARMA2 task. (d) Relationship between NMSE for Santa Fe and NARMA2 tasks with random QDRC and the designed QDRC. The green vertical and orange horizontal lines represent the NMSE values of the designed QDRC for the Santa Fe and NARMA tasks, respectively.

over the interval [0,1]. The input signal frequency was set to 1 GHz, and the peak intensity was 1.0×10^5. The target signal was a time-series signal delayed by d steps from the input signal. Using this input signal and the target output, we calculated the coefficient of determination between the input signal and output signal with the designed QDRC. Summing the coefficients of determination for delay tasks from $d = 1$ to $d = 20$, we estimated the memory capacity to be 7.2, which is consistent with time $t_{1/e}$ in case of weak intensity. This result indicates that the memory capacity of the QDRC can be estimated by measuring the fluorescence lifetime.

Precisely arranging QDs on the nanometer scale to form the designed QD network is challenging. However, in the experiment, one of the key advantages of our proposed method was utilized for selecting signals suitable for computing from among numerous signals. It was demonstrated that over 2,000 types of fluorescence signals can be acquired simultaneously by using a streak camera [15]. The signals measured by the streak camera correspond to the various fluorescence signals generated by QD networks, similar to the signals in Fig. 5 (a), and the design method described in the previous section can be applied directly to the experiment. Therefore, our proposed

method enables the selection of optimal signals for time-series prediction experimentally.

To evaluate prediction performance by using the rank of the reservoir state, a method using kernel quality was proposed [30]. However, the rankings depend on the task because the reservoir responses vary with the input data [29]. Furthermore, evaluating the rank of the matrix $\boldsymbol{F}$ constructed from the fluorescence signals generated when a single pulse is irradiated onto the QD networks leads to an estimation of the prediction performance for any task. This implies that the performance of the QDRC can be assessed using a single pulse and not an encoded pulse sequence. The designed QDRC can be utilized across a broad range of data prediction tasks, although non-designed QDRCs demonstrate more accuracy for specific tasks. The proposed method proves useful when the properties of the task to be solved are unknown in advance. If the target data is predetermined, the rigorous arrangement of QDs following the design optimizes performance in the QDRC [36].

5. Conclusion

In this paper, we proposed a method for designing QD networks that enhance the prediction performance of QDRC. We constructed a mathematical model of the energy state of the QD, accounting for FRET and level occupancy effects, to reproduce the fluorescence signals generated by numerous QD networks. We confirmed that the fluorescence signals in the numerical simulation are modulated depending on the irradiation conditions and the density of QDs, exhibiting characteristics similar to experimental results. We designed QD networks to generate signals that significantly contribute to the prediction of time-series data. By evaluating the rank of the matrix representing the signals generated in the numerical simulation, the QD networks to be designed were identified. The QDRC with the designed QD networks predicts time-series data with higher accuracy than those with randomly-selected QD networks. The performance of the designed QDRC is independent of the properties of the time-series data and can be utilized in diverse fields. Our method expands the capability of QD networks and contributes to the experimental development of QDRC. It is expected that the designed QDRC will enable the prediction of a wide range of time-series data, including chaotic behavior in nature.

Funding. This work was supported by JST KAKENHI Grant Number JP20H02657 and JP20H05890, JST CREST Grant Number JPMJCR18K2, and Konica Minolta Imaging Science Encouragement Award.

Acknowledgments. The authors would thank Masaki Nakagara, Fukuoka Institute of Technology and Naoya Tate, Kyushu Univdersity for informative discussions on the mathematical model.

Disclosures. The authors declare no conflicts of interest.

Data Availability. Data underlying the results presented in this paper are not publicly available at this time but may be obtained from the authors upon reasonable request.

References

1. M. M. Barroso, "Quantum dots in cell biology," J. Histochem. & Cytochem. **59**, 237–251 (2011).
2. J. Sobhanan, J. V. Rival, A. Anas, *et al.*, "Luminescent quantum dots: Synthesis, optical properties, bioimaging and toxicity," Adv. Drug Deliv. Rev. **197**, 114830 (2023).
3. B. Bajorowicz, M. P. Kobylański, A. Gołąbiewska, *et al.*, "Quantum dot-decorated semiconductor micro- and nanoparticles: A review of their synthesis, characterization and application in photocatalysis," Adv. Colloid Interface Sci. **256**, 352–372 (2018).
4. M. Zhang, J. Yue, R. Cui, *et al.*, "Bright quantum dots emitting at 1,600 nm in the nir-iib window for deep tissue fluorescence imaging," Proc. National Acad. Sci. **115**, 6590–6595 (2018).
5. U. Resch-Genger, M. Grabolle, S. Cavaliere-Jaricot, *et al.*, "Quantum dots versus organic dyes as fluorescent labels," Nat. Methods **5**, 763–775 (2008).
6. M. Bruchez, M. Moronne, P. Gin, *et al.*, "Semiconductor nanocrystals as fluorescent biological labels," Science **281**, 2013–2016 (1998).
7. I. L. Medintz and N. Hildebrandt, *FRET-Förster Resonance Energy Transfer: From Theory to Applications* (John Wiley & Sons, 2013).

8. K. F. Chou and A. M. Dennis, "Förster resonance energy transfer between quantum dot donors and quantum dot acceptors," Sensors **15**, 13288–13325 (2015).
9. N. Kholmicheva, P. Moroz, H. Eckard, *et al.*, "Energy transfer in quantum dot solids," ACS Energy Lett. **2**, 154–160 (2017).
10. T. Nishimura, Y. Ogura, and J. Tanida, "Fluorescence resonance energy transfer-based molecular logic circuit using a DNA scaffold," Appl. Phys. Lett. **101**, 233703 (2012).
11. J. C. Claussen, N. Hildebrandt, K. Susumu, *et al.*, "Complex logic functions implemented with quantum dot bionanophotonic circuits," ACS Appl. Mater. & Interfaces **6**, 3771–3778 (2014).
12. S. Wang, A. R. Lebeck, and C. Dwyer, "Nanoscale resonance energy transfer-based devices for probabilistic computing," IEEE Micro **35**, 72–84 (2015).
13. S. Shimomura, T. Nishimura, Y. Miyata, *et al.*, "Spectral and temporal optical signal generation using randomly distributed quantum dots," Opt. Rev. **27**, 264–269 (2020).
14. N. Tate, Y. Miyata, S. ichi Sakai, *et al.*, "Quantitative analysis of nonlinear optical input/output of a quantum-dot network based on the echo state property," Opt. Express **30**, 14669–14676 (2022).
15. N. Tate, S. Yamaguchi, S. Sakai, *et al.*, "Demonstration of quantum dot reservoir computing based on spatio-temporal optical processing," Appl. Opt. **63**, G30–G36 (2024).
16. N. Tate, M. Naruse, W. Nomura, *et al.*, "Demonstration of modulatable optical near-field interactions between dispersed resonant quantum dots," Opt. Express **19**, 18260–18271 (2011).
17. W. Nomura, T. Yatsui, T. Kawazoe, *et al.*, "Direct observation of optical excitation transfer based on resonant optical near-field interaction," Appl. Phys. B **107**, 257–262 (2012).
18. K. Vandoorne, P. Mechet, T. Van Vaerenbergh, *et al.*, "Experimental demonstration of reservoir computing on a silicon photonics chip," Nat. Commun. **5**, 3541 (2014).
19. D. Brunner, M. C. Soriano, C. R. Mirasso, and I. Fischer, "Parallel photonic information processing at gigabyte per second data rates using transient states," Nat. Commun. **4**, 1364 (2013).
20. M. Lukoševičius and H. Jaeger, "Reservoir computing approaches to recurrent neural network training," Comput. science review **3**, 127–149 (2009).
21. M. Nakagawa, Y. Miyata, N. Tate, *et al.*, "Spatiotemporal model for fret networks with multiple donors and acceptors: multicomponent exponential decay derived from the master equation," J. Opt. Soc. Am. B **38**, 294–299 (2021).
22. S. Wang, R. Vyas, and C. Dwyer, "Fluorescent taggants with temporally coded signatures," Opt. express **24**, 15528–15545 (2016).
23. V. Klimov, A. Mikhailovsky, S. Xu, *et al.*, "Optical gain and stimulated emission in nanocrystal quantum dots," science **290**, 314–317 (2000).
24. A. Zrenner, E. Beham, S. Stufler, *et al.*, "Coherent properties of a two-level system based on a quantum-dot photodiode," Nature **418**, 612–614 (2002).
25. F. de Sales, J. Cruz, S. da Silva, *et al.*, "Coupled rate equation modeling of self-assembled quantum dot photoluminescence," Microelectron. J. **34**, 705–707 (2003). The Fourth International Conference on Low Dimensional Structures and Devices.
26. H. M. Watrob, C.-P. Pan, and M. D. Barkley, "Two-step fret as a structural tool," J. Am. Chem. Soc. **125**, 7336–7343 (2003).
27. Y.-S. Park, W. K. Bae, T. Baker, *et al.*, "Effect of auger recombination on lasing in heterostructured quantum dots with engineered core/shell interfaces," Nano Lett. **15**, 7319–7328 (2015).
28. V. I. Klimov, A. A. Mikhailovsky, D. W. McBranch, *et al.*, "Quantization of multiparticle auger rates in semiconductor quantum dots," Science **287**, 1011–1013 (2000).
29. J. Chrol-Cannon and Y. Jin, "On the correlation between reservoir metrics and performance for time series classification under the influence of synaptic plasticity," PLOS ONE **9**, 1–8 (2014).
30. R. Legenstein and W. Maass, "Edge of chaos and prediction of computational performance for neural circuit models," Neural Networks **20**, 323–334 (2007). Echo State Networks and Liquid State Machines.
31. L. Büsing, B. Schrauwen, and R. Legenstein, "Connectivity, Dynamics, and Memory in Reservoir Computing with Binary and Analog Neurons," Neural Comput. **22**, 1272–1311 (2010).
32. L. Junges and J. A. Gallas, "Intricate routes to chaos in the mackey–glass delayed feedback system," Phys. Lett. A **376**, 2109–2116 (2012).
33. A. Weigend and N. Gershenfeld, "Results of the time series prediction competition at the santa fe institute," in *IEEE International Conference on Neural Networks,* (1993), pp. 1786–1793 vol.3.
34. A. Atiya and A. Parlos, "New results on recurrent network training: unifying the algorithms and accelerating convergence," IEEE Trans. on Neural Networks **11**, 697–709 (2000).
35. H. Jaeger, *Short term memory in echo state networks*, GMD Report; 152 (GMD Forschungszentrum Informationstechnik, 2001).
36. O. Lee, T. Wei, K. D. Stenning, *et al.*, "Task-adaptive physical reservoir computing," Nat. Mater. **23**, 79–87 (2024).